High-Speed Spatial–Spectral Encoding with PEPSI and Spiral MRSI

Stefan Posse[1] & Xiaoping Hu[2]

[1] *University of New Mexico School of Medicine, Albuquerque, NM, USA*
[2] *Georgia Tech and Emory University, Atlanta, GA, USA*

Magnetic resonance spectroscopic imaging (MRSI), also called spectroscopic imaging (SI) or chemical shift imaging (CSI), has become a valuable tool for mapping metabolites in human brain, prostate, breast, and other organs. However, commercially available phase-encoded MRSI methods require long acquisition times, which limit clinical applications. High-speed MRSI methods based on echo-planar and spiral encoding have become viable alternatives to conventional proton MRSI for clinical research applications that demand short scan times, large volume coverage, and high spatial resolution. This article describes the principles of proton echo-planar spectroscopic imaging (PEPSI) and spiral MRSI, with an emphasis on designing robust data acquisition and reconstruction methods for routine applications. Covered topics include: ramp sampling, gridding, off-resonance correction, even–odd echo editing of PEPSI data, sensitivity comparison with conventional phase-encoded MRSI, gradient and receiver hardware requirements, sensitivity to eddy currents and magnetic field inhomogeneity, and variable density *k*-space sampling. Advanced topics include: the integration of acceleration techniques, such as parallel imaging and compressed sensing that take advantage of using large-scale array coils; the selection of volume prelocalization techniques; and implementation at different field strengths. The article will conclude with selected research applications in human brain that highlight the advantages of high-speed MRSI.

Keywords: MR spectroscopic imaging, chemical shift imaging, proton echo-planar spectroscopic imaging, echo-planar spectroscopic imaging, spiral spectroscopic imaging, parallel imaging, compressed sensing, human, brain, breast

How to cite this article:
eMagRes, 2015, Vol 4: 587–600. DOI 10.1002/9780470034590.emrstm1439

Introduction

Magnetic resonance spectroscopic imaging (MRSI) is a widely available tool for routine clinical imaging and for both preclinical and clinical research. It can be used for spatially mapping multiple tissue metabolite signals in vivo to characterize neurological, psychiatric, and metabolic disease.[1] Phase-encoded MRSI, which was first described by Brown *et al.*[2] in 1982 and further developed by Maudsley *et al.*[3] in 1983, remains the most widely used commercially available MRSI method despite the slow encoding speed that requires a separate acquisition for each phase-encoding step. Volumetric acquisitions even with a moderate matrix size would require encoding times that are quite unacceptable for human studies. For example, to acquire a $32 \times 32 \times 8$ matrix using a sequence repetition time (TR) of 1 s with elliptical sampling would require 46 min of encoding time. Typical conventional raw two-dimensional (2D) MRSI data matrix sizes used in clinical research studies are much smaller: 16×16, 24×24, or 32×32 data points, but still require substantial acquisition times. This slow encoding efficiency is a limitation for clinical applications, particularly when prelocalization methods have improved to enable acquisitions from larger volumes, and where increasingly available and sensitive large-scale array coils permit higher spatial resolution.

Acceleration of ^{1}H-MRSI to decrease scan time, signal-to-noise ratio (SNR)-permitting, in order to increase volume coverage, and to reduce motion sensitivity is highly desirable for integrating MRS into clinical protocols. High-speed MRSI also enables integration of high-resolution 2D MRS methods, such as correlation spectroscopy (COSY)[4] and J-resolved spectroscopy[5] (see ***2D MRS***), three dimensional (3D) spatial mapping of gamma-amino-butyric-acid (GABA) using spectral editing[6] (see ***Spectral editing in MRS***) and implementation of multistep phase-cycling schemes. The rapidly expanding field of hyperpolarized MRI has invigorated the development of ultrafast MRSI-encoding schemes with the goals of minimizing image blurring and maximizing the efficient use of the rapidly decaying magnetization (see ***CSI and SENSE CSI***).

High-speed MRSI in the form of echo-planar spectroscopic imaging (EPSI) using rapidly switching gradients during the data spectroscopic acquisition to interleave spatial and spectral encoding was introduced in the late 1980s by Nobel laureate Peter Mansfield.[7] At that time, this approach, which in its most advanced implementation would yield an entire 3D spectroscopic image in a single shot, was a radical departure from traditional MRSI. It has taken a long time to develop a practical implementation of the method on preclinical and clinical MRI scanners, primarily due to hardware limitations of the gradients that limited initial feasibility studies.[8,9] A long-standing dogma

was that switching a gradient on during a spectroscopic acquisition would corrupt the fragile spectroscopic signal. Practical implementations on clinical scanners benefitted from the rapid development of high-performance actively-shielded gradient systems and in the mid-1990s, the first demonstration of proton echo-planar spectroscopic imaging (PEPSI) in the human brain by Posse *et al.*,[10,11] showed orders-of-magnitude faster encoding efficiencies compared with conventional MRSI, yet with similar sensitivity per unit time and unit volume and spectral quality. This stimulated further method development during the subsequent decade.[12,13] Spiral MRSI, which makes efficient use of the gradient performance on clinical scanners and offers faster acceleration than echo-planar-based techniques due to the higher efficiency of the spiral trajectory, was introduced a few years later by Adalsteinsson *et al.*[14]

The development of high-speed MRSI methods has now reached a level of maturity and reliability such that a growing number of research studies have demonstrated its utility for applications in brain and body, predominantly in humans.[1] Echo-planar-based methods offer the most frequently used high-speed alternative to MRSI methods for human brain applications due to their robust localization performance. Implementation at field strengths ranging from 1.5 to 7 T[15]; acquisition at very short echo-times (TE = 15 ms, for example) for mapping of J-coupled metabolites in human brain in clinically feasible scan times of less than 5 min[1,16]; integration of J-editing[5]; and the feasibility of whole brain coverage[17] have all been demonstrated. The combination of PEPSI with parallel imaging (see ***CSI and SENSE CSI***) has enabled very fast encoding speeds.[18–21] Spiral MRSI provides faster acceleration and greater flexibility in encoding *k*-space than echo-planar-based methods, and recent advances in method development demonstrate its utility for clinical research studies.[22]

Spatial–Spectral Encoding and Reconstruction

Proton Echo Planar Spectroscopic Imaging

Basic Principles. Echo-planar spatial–spectral encoding utilizes a train of echo-planar readout gradients with alternating polarity during the spectroscopic readout to create a series of gradient echoes that interleave spatial encoding along the gradient direction into the spectral-encoding process. The relatively narrow spectral width of the proton spectrum (~8 ppm) enables interleaving of an entire readout gradient during the spectroscopic dwell time (500–1000 μs) and a spatial resolution of several millimeters that is commensurate with the sensitivity constraints of ^{1}H-MRSI at high field strength (Figure 1a). The train of echo-planar readout gradients generates a series of even and odd gradient echoes (Figure 1b) and encodes k_x–t-space in a zig-zag trajectory that interleaves k_x encoding between spectroscopic acquisition points (Figure 2). The acceleration of spatial encoding is thus proportional to the number of pixels n_x that are encoded along the readout direction. Interleaving of spatial and spectral information using echo-planar gradients takes advantage of the different time scales at which spatial and spectral information evolve. The spacing of the readout gradients (Δt) determines the encoded spectral width in the reconstructed spectra ($1/\Delta t$). Spatial encoding requires an n_x times increase in the acquisition bandwidth compared with conventional MRSI, which results in a pixel bandwidth that encompasses the entire spectroscopic bandwidth and thus provides separation of spatial and spectral information. The duration of the entire readout train with N gradients ($N^{*}\Delta t$) determines the digital spectral resolution in the reconstructed spectra ($1/(N^{*}\Delta t)$).

Reordering the data into a 2D matrix (k_x, t) and application of a 2D Fourier transform (FT) reconstructs the localized spectra that are spatially resolved along the readout direction. In the original implementation of PEPSI, the application of echo-planar encoding along the readout direction is combined with conventional phase encoding along the second (and third) spatial dimensions. It is thus advantageous to apply the echo-planar readout gradients along the largest image matrix dimension unless hardware constraints dictate otherwise. Given adequate gradient performance or sufficiently narrow spectral width, it is possible to further accelerate this single-shot spatial–spectral encoding scheme by interleaving an additional spatial dimension, which will be described in the section titled 'Coil Arrays and Parallel Imaging'.

Ramp Sampling and Off-resonance Correction. Echo-planar gradient encoding can be implemented using linear gradient ramps, which provide the shortest ramp times. The use of sinusoidal gradient ramps can reduce eddy currents compared with linear ramps, but requires longer ramp times. Data acquisition during the gradient ramps shortens the dead time in the data acquisition and decreases peak gradient amplitudes and sampling rates, thus increasing acquisition efficiency. To obtain equidistant *k*-space sampling during gradient ramping, it is necessary to either dynamically adjust the analog-to-digital converter's (ADC) sampling rate as a function of gradient amplitude or to use a constant ADC sampling rate and convolution interpolation, also known as gridding, which is typically implemented using a Kaiser–Bessel convolution kernel. Twofold oversampling of the *k*-space data and truncation of the reconstructed frequency spectrum ensures that filter nonlinearities at the edges of the spectrum are avoided. During ramp sampling, the chemical shift displacement becomes a function of *k*-space encoding. If uncorrected, high *k*-space information sampled at the beginning of the ramp-up of the readout gradient can become significantly displaced as compared to lower *k*-space information encoded at the end of the ramp-up phase. This may cause edges of chemically shifted species (e.g., peripheral lipids) to be strongly displaced. This displacement can be limited by interrupting data acquisition during periods of low readout gradient amplitude, i.e., using delayed ramp sampling at the beginning of the gradient ramp-up and by ending ramp sampling before the end of the gradient ramp-down, at the expense of a small loss in SNR. *k*-Space apodization using sine-bell or a Fermi filter also attenuates the effects of ramp sampling.

The chemical shift displacement in the readout direction is small due to the narrow spectral range of the major resonances of the proton spectrum (less than a $^{1}/_{2}$-voxel between water and

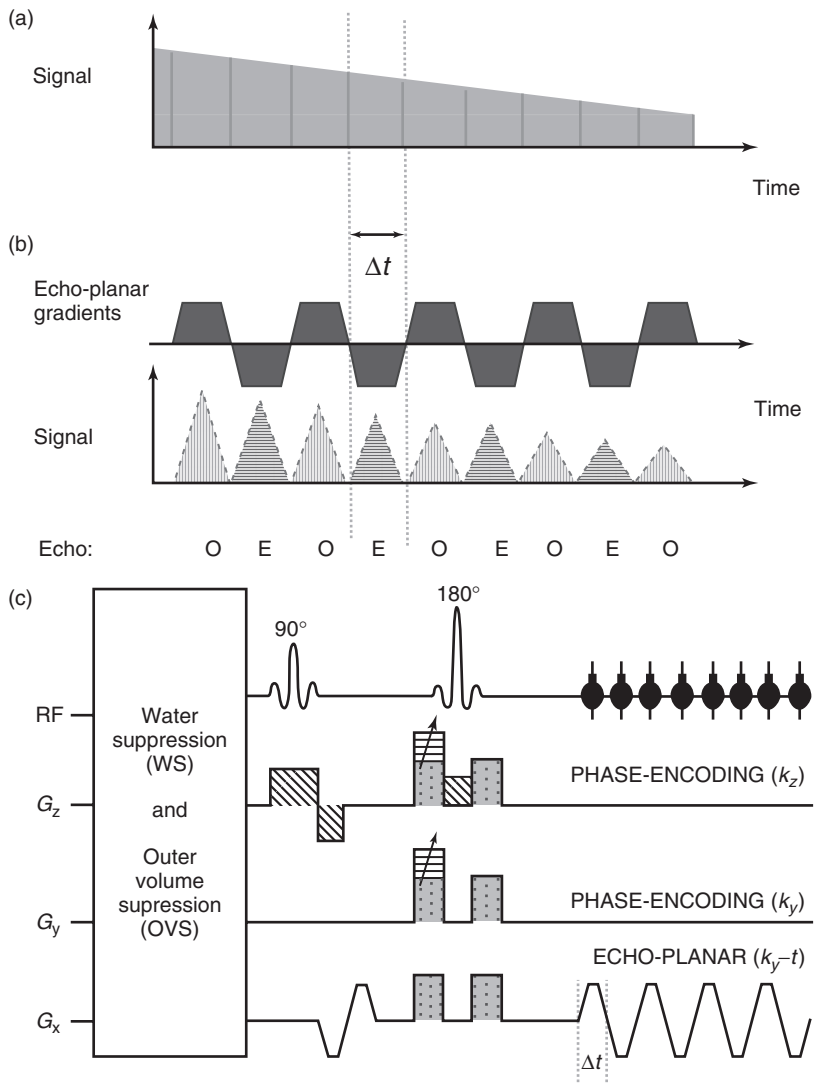

Figure 1. Echo-planar spatial–spectral encoding. (a) Conventional MRSI acquisition with sampling points indicated by red lines. The spacing between sampling points is the spectroscopic dwell time (Δt). (b) Interleaving of pairs of echo-planar readout gradients into the spectroscopic acquisition creates a series of even and odd gradient echoes. (c) 3D-PEPSI pulse sequence with water-suppression (WS), outer-volume-suppression (OVS), spin-echo RF excitation, and phase encodes on G_y and G_z for y and z encoding and trapezoidal G_x gradient for simultaneous encoding of x and f

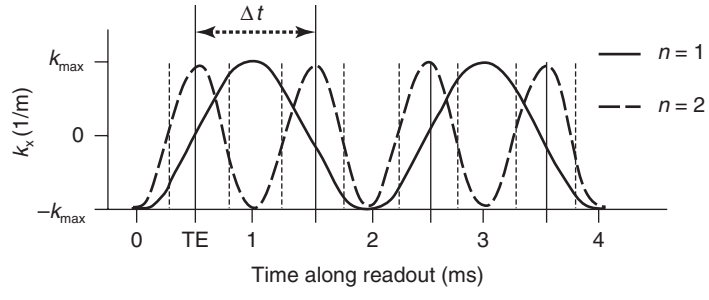

Figure 2. k-Space encoding with different oversampling ratios (n). The time interval Δt determines the desired spectral width $1/\Delta t$ in the reconstructed spectra. The straight lines represent the isotemporal k-space planes to which the measured data is interpolated

n-acetyl aspartate, NAA). Correction of this chemical shift displacement can be implemented in postprocessing using a phase ramp in the Fourier (i.e., spectral) domain that depends on the *k*-space position (see section titled 'Temporal Alignment'). This corresponds to sinc interpolation in the time domain onto isotemporal *k*-space planes (Figure 2). Note that to obtain isotemporal data at TE, it is necessary to start data collection before TE such that all *k*-space points have data before TE.

Spatial–Spectral Reconstruction and the Point-Spread-Function. The echo-planar readout gradient train creates a series of gradient echoes that are modulated by chemical shift evolution and relaxation. Reformatting these data into a 2D matrix creates a data format that is equivalent to that of conventional one-dimensional phase-encoded MRSI. However, direct FT across the even and odd echoes would lead to severe ghosting artifacts in the spectral domain due to echo asymmetries in gradient switching, eddy current-induced signal distortions, and inhomogeneity-related signal displacements in $k-t$-space, which lead to increasing shifts of the even and odd gradient echoes with increasing spectral encoding time that alternate along the readout direction.

Separate reconstruction of the data from even and odd echo acquisitions and combination of the two data sets after inverting the readout direction for the odd echo data is a robust reconstruction method that avoids ghosting altogether.[10] This approach requires doubling of the inversion frequency of the gradients to achieve twofold oversampling in the spectral domain to maintain the reconstructed spectral bandwidth (Figure 2). Higher-order oversampling can be used to further reduce chemical shift displacement at the expense of acquisition efficiency (Figure 3). The flyback gradient scheme, which uses only the even gradients for spatial encoding and short gradient pulses with maximum slew rate for refocusing, has been proposed as an alternative approach to avoid eddy current effects and ghosting,[23] but sensitivity is reduced due to gaps in data acquisition during the flyback gradient. The interlaced FT, which utilizes both even and odd echo data to reconstruct a full bandwidth spectrum, has been introduced as an alternative to minimize ghosting in the frequency domain.[12,24] It requires a precise measurement of the time delays between even and odd echoes. In the presence of local magnetic field inhomogeneity, it requires a correction of the diverging echo positions with increasing spectral encoding time, which become challenging if the local gradients are nonlinear and the gradient echoes disperse in $k-t$-space (group spin echo displacement).[25]

The point-spread function (PSF) of PEPSI and the sensitivity to magnetic field inhomogeneity are identical to those of conventional phase-encoded MRSI at identical spatial and spectral resolution. Geometrical displacement artifacts due to the interference of local gradients with the echo-planar readout gradients are typically quite small due to the high amplitudes of the readout gradients. PEPSI is compatible with elliptical k_y-k_z-space encoding, which reduces measurement time by as much as 50% in the case of 3D encoding, and with weighted averaging to further reduce scan time, albeit at the expense of having an increased noise variance of high *k*-space versus low *k*-space data.

Sensitivity. As has been shown theoretically and experimentally, the SNR per unit volume and unit time in PEPSI is comparable to conventional spectroscopic imaging at the same bandwidth per data point, provided that ramp sampling is used.[15,26] The reader can intuitively understand this by considering the following one-dimensional case. When echo-planar gradients are applied, the readout bandwidth increases with the number of encoded voxels (N), resulting in a concomitant $\sqrt{N}$ increase in noise in a single excitation. When using N averages to match the acquisition time of conventional phase-encoded acquisition, the SNR increases by $\sqrt{N}$ to match the SNR of the phase-encoded acquisition.

To assess the influence of the readout gradient waveform on SNR, we compare the noise variance of a trapezoidal waveform with the noise variance of an ideal rectangular

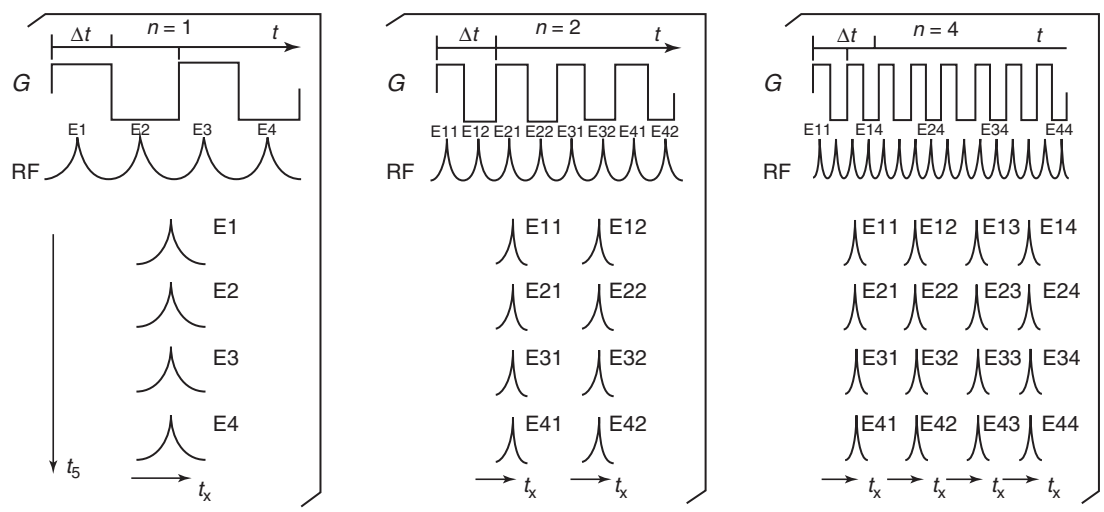

Figure 3. Editing of even and odd gradient echoes (E) with different oversampling ratios (n). The time interval Δt determines the desired spectral width $1/\Delta t$ in the reconstructed spectra. Reformatting into 2D data matrices and two-dimensional FT provides series of spatially localized spectra. Spectral data series obtained with oversampling are combined

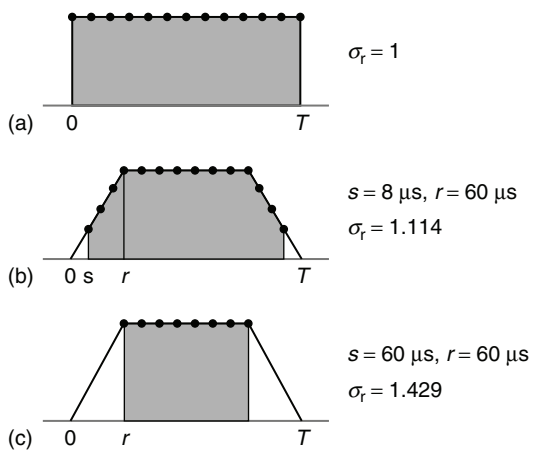

Figure 4. Noise variance for different gradient waveforms and sampling schemes (dots) (*r*, ramp time; *s*, ADC ramp sampling delay; and *T*, total gradient duration). (a) Ideal rectangular gradient. (b) Trapezoidal gradient with ramp sampling. (c) Trapezoidal gradient without ramp sampling. The gradient duration *T* is identical in all cases (460 μs) to achieve the same spectral width. The noise variance for each case is normalized to the noise variance of the ideal rectangular gradient. (Reproduced with permission from Ref. 15. © John Wiley & Sons, Ltd., 2006)

gradient (Figure 4). A general formula to compute the noise variance in the reconstructed image for a variety of possible waveforms that was derived by Pipe and Duerk[27] is given by:

$$\sigma_i = \frac{\sigma^2 \int_{t_0}^{t_1} G_i^2(t)\mathrm{d}t}{\left(\int_{t_0}^{t_1} G_i(t)\,\mathrm{d}t\right)^2} \qquad (1)$$

where $G_i(t)$ is the waveform type i, σ the standard deviation of the white noise, and $[t_0, t_1]$ the sampling interval. σ also corresponds to the noise variance in conventional phase-encoded MRSI, when using the same measurement time and voxel size. Using, for example, a 460 μs trapezoidal readout gradient with ramp sampling, 60 μs ramp time, and 8 μs ADC ramp sampling delay, the increase in noise variance is 11.4% with respect to conventional phase encoding. Without ramp sampling, the increase is 42.9%. Accordingly, the SNR loss in PEPSI caused by the interruptions of the acquisition due to gradient switching is significantly reduced when using ramp sampling with regridding reconstruction. Experimentally, the SNR per unit volume and unit time of PEPSI with ramp sampling was found to be similar to that of conventional phase-encoded MRSI, as predicted theoretically.[26] There is still a small loss in SNR even with full ramp sampling (the increase in noise variance in the above example is 10.7% with respect to conventional phase encoding).

The efficiency of the echo-planar-encoding scheme decreases with increasing spatial resolution and spectral bandwidth due to increased ramp sampling. Ramp sampling also introduces colored noise in the reconstructed spectroscopic image due to the *k*-space-dependent noise bandwidth during ramp sampling, which enhances the SNR of detecting sharp edges, for example, from residual peripheral lipids. At high spatial resolution and spectral bandwidth, it may be necessary to use spectral interleaving (see ***Direct Water–Fat Imaging Methods: Chemical Shift-Selective and Chemical Shift-Encoded MRI***) to maintain SNR.

Gradient and Receiver Hardware Requirements. The design of an echo-planar trajectory, following the principles for echo-planar imaging, has to take into consideration hardware constraints that include: the gradient slew rate; the gradient duty cycle that may depend on the gradient axis; acoustic gradient resonances that must be avoided to prevent gradient damage; and short- and long-term eddy currents that will be more severe for off-center acquisition, gradient and ADC digitization raster times, data size and data acquisition rate limitations, as well as physiological stimulation limits. In case of continuous data acquisition, it is necessary to consider the maximum supported ADC vector size. In the case of separate ADC events for each readout gradient, it may be necessary to insert a wait time between ADC events to avoid buffer overflows in the receive chain. PEPSI using even–odd echo separation is remarkably resilient against eddy current artifacts that predominantly manifest as distortions at the base of the spectral peaks. However, it is sensitive to frequency drifts due to gradient heating, which result in spectral line broadening and can be corrected using frequency drift compensation.[28]

High-speed Spectroscopic Imaging using Spiral *k*-Space Trajectory

Basic Principles. In this method, which was introduced by Adalsteinsson *et al.*,[14,29] time-varying gradients are applied in both spatial encoding directions (*x* and *y*) during data acquisition, such that the *k*-space is covered along a spiral trajectory. To capture the temporal evolution of the MR signal, the spiral gradient waveforms are repeated multiple times after each excitation, resulting in temporal sampling of the spatially encoded nuclear magnetic resonance (NMR) signal. At the end of each spiral trajectory, appropriate rewinding gradients are applied so that the *k*-space trajectory starts from zero for the next repetition. In principle, the spiral strategy can acquire spectroscopic data in one shot as no phase encoding is necessary, and the total scan times can be very short (of the order of seconds) but single shot approaches are usually not practical due to limitation of bandwidth imposed by the time required to complete the spiral trajectory. In practice, spiral MRSI is usually achieved with *k*-space and/or time interleaving (see ***Direct Water–Fat Imaging Methods: Chemical Shift-Selective and Chemical Shift-Encoded MRI***). In addition, the spiral trajectory permits a natural vehicle for varying sampling density, a feature that can be taken advantage of in spectroscopic imaging. The following subsections will describe the principles and practical implementation of spiral trajectory, reconstruction algorithms, and application of variable density spiral.

Spiral MRSI Pulse Sequence. The sequence diagram for spiral MRSI is shown in Figure 5. Alternating gradients are applied along both the spatial directions during the acquisition of a spin-echo after slice-selective excitation. The gradients are

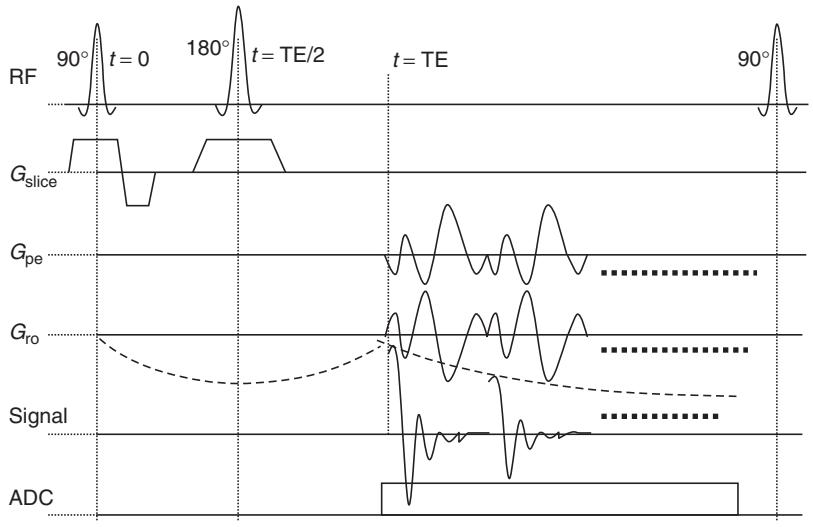

Figure 5. Pulse sequence diagram for spiral MRSI

rewound and reapplied to capture the temporal evolution of the spatially encoded NMR signal. The total time required for the application of the spiral gradient waveform and the rewinding gradient determines the temporal sampling interval, Δt. With a single-shot acquisition scheme, each k-space point can at best have a temporal resolution of Δt or a maximum spectral bandwidth of $1/\Delta t$. However, temporal interleaves can be used to achieve a higher bandwidth (see ***Direct Water–Fat Imaging Methods: Chemical Shift-Selective and Chemical Shift-Encoded MRI***). With temporal interleave, multiple shots are used, and the starting times for the spiral waveform are temporally shifted with the smallest shift corresponding to the desired temporal resolution. In this case, the minimum number of shots required is determined by the ratio of Δt over the desired sampling interval. Alternatively, k-space interleaving can be designed to shorten the spiral trajectory needed for each shot, resulting in a smaller Δt. As multiple averages are often needed in MRSI to achieve desired SNR, it is not a sacrifice to use interleaving in spiral MRSI. The total scan time is a product of the number of interleaves (temporal and k-space), the number of averages, and the repetition time (TR). The data acquisition is done along the $(\vec{k}, t)$ trajectory: the projection of this 3D trajectory onto the k_x–t plane is shown in Figure 6.

Spiral Trajectory Design. Like in anatomic imaging, a spiral k-space trajectory for spectroscopic imaging is designed to follow an Archimedean spiral in which the radius at any point on the spiral is proportional to the total angle traced out to that point from the beginning of the spiral. A spiral k-space trajectory that starts from the origin and spirals out can be represented as $\vec{k}(t) = k_{\max}(\rho(t)/T)\exp(j\omega\tau(t))$, where T is the total time for the spiral trajectory, $k_{\max}$ is the maximum value of the radial distance from the origin of the spiral that will be reached at $\rho(t) = T$, ω is the angular frequency of the spiral, and $\tau(t)$ is the total angle traced by the spiral trajectory. For a spiral with constant angular velocity, we set $\tau(t) = \rho(t) = t$.[30] With $\tau(t) = \rho(t) = \sqrt{t}$, we have a constant linear velocity spiral.[31] A variable density trajectory[32] can be obtained by varying the ratio of the derivatives $(d\tau/dt)/(d\rho/dt)$. Note that a spiral-in trajectory can be achieved using $\vec{k}(t) = k_{\max}(1 - \rho(t)/T)\exp(j\omega\tau(t))$ starting from $k_{\max}$ and ending at the k-space origin. Time-varying gradients are applied along two spatial-encoding directions, say x and y, during data acquisition. The gradients required to trace a desired trajectory in k-space can be generated using $d\vec{k}/dt = \gamma\vec{G}(t)$, where $\vec{G}(t) = G_x(t) + jG_y(t)$ and $k(t) = k_x(t) + jk_y(t)$ are represented in complex notation ($j = \sqrt{-1}$). For the constant angular velocity case, where $\tau(t) = \rho(t) = t$,

$$\vec{G}(t) = \frac{1}{\gamma}\frac{d\vec{k}}{dt} = \frac{k_{\max}}{\gamma T}\exp(j\omega t) + j\frac{k_{\max}}{\gamma T}\omega t\exp(j\omega t)$$
$$\approx j\frac{k_{\max}}{\gamma T}\omega t\exp(j\omega t),$$

or $G_x(t) = \frac{k_{\max}}{\gamma T}[\cos(\omega t) + \omega t\sin(\omega t)]$ and $G_y(t) = \frac{k_{\max}}{\gamma T}[\sin(\omega t) + \omega t\cos(\omega t)]$.

Constant angular velocity spirals are not optimal for SNR and scan-time because k-space is sampled nonuniformly, and the maximum gradient amplitude is reached only at the end of a spiral. For constant linear-velocity spirals, $\tau(t) = \sqrt{t}$, and $\vec{G}(t) = \frac{1}{\gamma}\frac{d\vec{k}}{dt} = \frac{k_{\max}}{2\gamma T}\frac{1}{\sqrt{t}}\exp(j\omega t) + j\frac{k_{\max}}{2\gamma T}\omega\exp(j\omega t) \approx j\frac{k_{\max}}{2\gamma T}\omega\exp(j\omega t)$, ignoring the singularity at $t = 0$. In this case, the gradient can take maximum amplitude and remains constant for the entire duration, while the k-space is sampled at a uniform density.

In practice, scanner gradients have to be applied with rise time constraints: a gradient cannot start at a high amplitude and needs to be ramped up to the full amplitude. In addition, the spiral trajectory is often a combination of the two types of spirals. A numerical approach similar to that suggested by Hardy and Cline[33] is often used to incorporate the effects of gradient hardware constraints on the generation of optimal gradients. The basic steps of the numerical gradient generation procedure are detailed below. The parameters used in the description are FOV (field-of-view), N (matrix size), N_{seg}

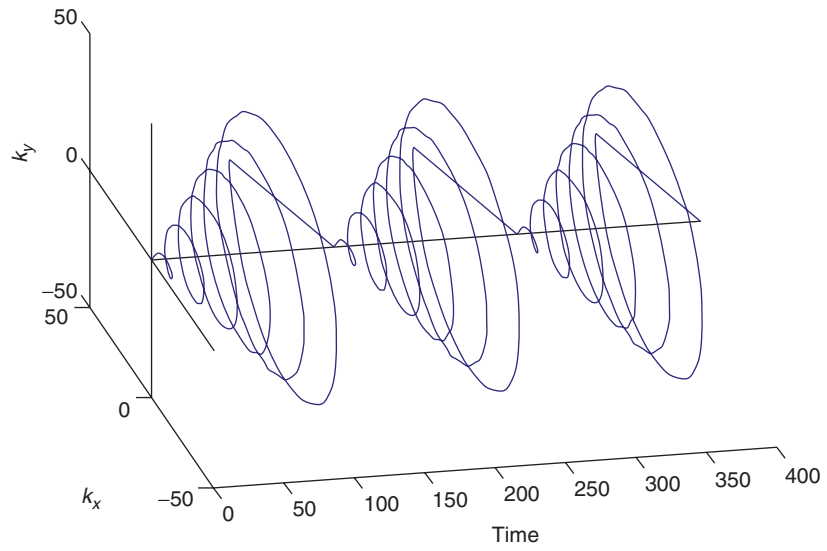

Figure 6. The k–t trajectory for spiral MRSI illustrated for three time points

(number of interleaves), G_{max} (maximum gradient amplitude), $T_{G_{max}}$ (minimum rise time to reach G_{max}), δt (incremental time duration for a gradient step), N_r (number of turns in spiral $= N/(2N_{seg})$), T (a final value of $\tau(t)$) that determines the angular velocity (ω) of the spiral, and *vd* (variable density profile, which will be relevant later).

1. Initialization: $\tau(-1) = \rho(-1) = -\delta t$; $\tau(0) = \rho(0) = 0$; $\tau(+1) = \rho(+1) = \delta t$. Using these values compute the initial values of
   - **A.** k-space: $k(i) = \frac{N}{2\text{FOV}} \frac{\rho(i)}{T} \exp\left(j2\pi N_r \frac{\tau(i)}{T}\right)$ for $i = -1, 0, 1$.
   - **B.** gradient: $g(i) = \frac{1}{G_{max}} \frac{1}{\gamma\delta t}[k(i) - k(i-1)]$ for $i = 0,1$.
   - **C.** slew rate: $s(i) = \frac{T_{G_{max}}}{G_{max}} \frac{1}{\gamma(\delta t)^2}[k(i+1) - 2k(i) + k(i-1)]$ for $i = 0$.
2. Compute next τ and ρ: $\tau(i) = \tau(i-1) + 0.8 \cdot (\tau(i-1) - \tau(i-2)) + \eta\Delta t \times 10^{-4}$ and $\rho(i) = \rho(i-1) + 0.8 \cdot ((i-1) - \rho(i-2)) + (\eta\Delta t/vd(\tau(i)/T)) \times 10^{-4}$. Compute the values for $k(i)$, $g(i)$, and $s(i-1)$ using the equations in step 1. Increment η till either the slew rate limit $|s(i)| \geq 1$ or the gradient limit $|g(i)| \geq 1$ is reached. Separate slew rate and gradient limits can be used for the x and y directions separately for a single shot spiral ($N_{seg} = 1$).
3. Increment i and repeat step 2 until $k(i) \geq N/(2 \times \text{FOV})$ or some other termination criterion is reached.
4. Interleaves or different segments can be generated by rotating the generated gradient $g(i)$ by incremental angular steps of $2\pi/N_{seg}$.

Several spiral trajectory gradient generation methods have been reported by other investigators,[34–36] but are essentially the same basic idea as in Refs 31, 33 These methods try to optimize the generation of practical gradient trajectories by incorporating gradient hardware specifications in the gradient design procedure. Approximate analytical forms[37] can also be used for rapid gradient generation on the fly in acquisition systems.

Reconstruction.

Temporal Alignment Data are collected along the trajectory in $(\vec{k}, t)$ space, dictated by the applied gradients. With the evolution of time during each repetition of the spiral, the spectral and the spatial information are encoded in a mixed manner. Specifically, data acquired during application of time-varying gradients can be expressed in the equation below

$$M_{T'}(t, \vec{k}(t)) = \int_f \int_{\vec{r}} M_0(f, \vec{r}) \times \exp(-j2\pi\vec{k}(t)\vec{r}) \exp(-j2\pi ft) \times \exp\left(-\frac{t}{T_2^*(\vec{r}, \sigma)}\right) d^2\vec{r}df$$

where $M_{T'}(t, \vec{k}(t))$ is the measured transverse magnetization, $M_0(f, \vec{r})$ is the spatially resolved spectroscopic information, the first exponential is the spatial encoding phase, the second is the phase evolution due to inhomogeneity and chemical shift, and the third exponential describes the T_2^* weighting. Because $\vec{k}$ is a function of t, the second exponential also leads to a $\vec{k}$-dependent phase in the acquired signal when f is nonzero. The off-resonance effect leads to frequency-dependent shift in the reconstructed images, similar to chemical shift artifact. To obtain off-resonance artifact-free spatial reconstruction, spatial encoding and temporal evolution in the acquired data need to be separated. To this end, the data corresponding to each k-space point is shifted by an appropriate amount of time, by applying a linear phase in the Fourier space as

$$M_{T'}(\vec{k}, l\Delta t) = \text{FT}_f^{-1}\left\{\text{FT}_t\left\{M_{T'}\left(\vec{k}, t\right)\right\} \cdot \exp\left(-j\frac{2\pi}{T}\left(\frac{t\left(\vec{k}\right) - T_{seg}}{T_{seg}/N_{tseg}}\right)f\right)\right\},$$

where T_{seg} is the acquisition time for each interleave, N_{tseg} is the number of temporal interleaves, T is the total time for each free induction decay (FID), and $t(\vec{k})$ is the time of acquisition of a particular k-space point from the start of each acquisition. This procedure is applied for each sampled k-space point. Note that to obtain isotemporal k-space data at TE, it is necessary to start acquiring the data slightly before TE so that all k-space points have at least one point before TE. The above procedure is equivalent to sinc interpolation in the time domain and is exact because the spectral data is band-limited.

Gridding To use the fast Fourier transform (FFT) for spatial reconstruction, gridding[38,39] of the k-space data needs to be performed, respectively, for each sampled time point. Gridding consists of density compensation. The k-space measurements along isotemporal planes are compensated for density change with angular and radial k-space traversal, convolved with a Kaiser–Bessel window and resampled along a Cartesian grid. The Cartesian grid spacing is governed by the Nyquist sampling requirements: hence the high-density sampling in low k-space amounts to averaging of oversampled data. The density compensation is comprised of a product of two components: the density change with angular traversal along the spiral trajectory due to system constraints and the density change along the radial direction due to the dual density nature of the trajectory. The angular density weighting function is obtained from $d\tau/dt$ and the radial density function is obtained from $(d\tau/dt)/(d\rho/dt)$, which are parameters in the gradient generation procedure detailed above.

Variable Density Spiral MRSI. In spectroscopic imaging, truncation artifacts can be very severe due to limited coverage of k-space. This could be a limiting factor when imaging low levels of metabolites next to a high level of unwanted signal, such as that arising from an extra-cranial lipid signal from subcutaneous fat in proton MRSI of the brain. Various methods have been developed to reduce truncation artifacts in MRSI. One common approach is to apodize in the k-space or smooth in the spatial domain, which can be achieved either through post-processing or modified data acquisition.[40] k-Space apodization reduces truncation artifact to a great extent by reducing sidelobes of the PSF resulting from the truncation of k-space, at the expense of an increase in width of the PSF and loss of spatial resolution. To alleviate this problem, a wider apodization window can be used to compensate for the loss in spatial resolution. This is achieved by expanding the k-space coverage, which, however, generally leads to an increase in acquisition time. The k-space sampling density can be varied in a similar manner to the apodization function to reduce noise.[41,42] An efficient implementation of this strategy is achieved using a variable density-spiral trajectory with a sampling density that is the same as a Hamming window with twice the k-space coverage[43]: an approximately 15 dB reduction in magnitude of the first sidelobe may be obtained without sacrificing SNR or spatial resolution.

While apodization reduces ringing artifact to a reasonable extent, it is insufficient to reduce signal contamination from high-intensity areas, such as that arising from subcutaneous lipid signal in brain proton MRSI. For reducing contamination from areas of high signal intensity, a more effective approach is to capture the high-intensity areas with high-spatial resolution and low-signal areas with low-spatial resolution and reconstruct them properly with a so-called 'selective reconstruction'.[44] Such an approach was initially demonstrated with phase-encoded MRSI[44] and an echo-planar/phase-encoding MRSI hybrid.[45] It can be elegantly implemented with dual density spirals, wherein the low k-space is sampled with high density to achieve a high SNR, while the high k-space region is sampled at the Nyquist limit to achieve the highest k-space possible, as shown in Figure 7.[46] For in vivo applications of the dual density approach, a 30 dB reduction of the lipid signal contamination has been achieved, making it possible to acquire brain proton MRSI metabolite signals even near the skull.

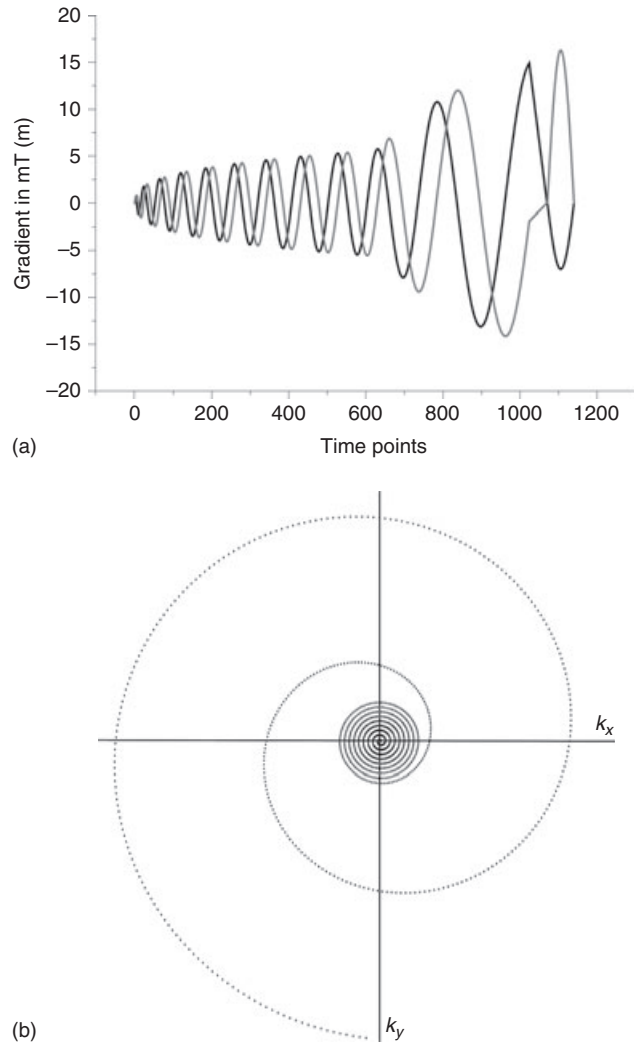

Figure 7. The dual density spiral gradient waveform (a) and k-space coverage (b) for one k-space interleave. (Reprinted from Magnetic Resonance Imaging, 20, 743; S. Sarkar, K. Heberlein and X. Hu, "Truncation artifact reduction in spectroscopic imaging using a dual-density spiral k-space trajectory" (2002), with permission from Elsevier)

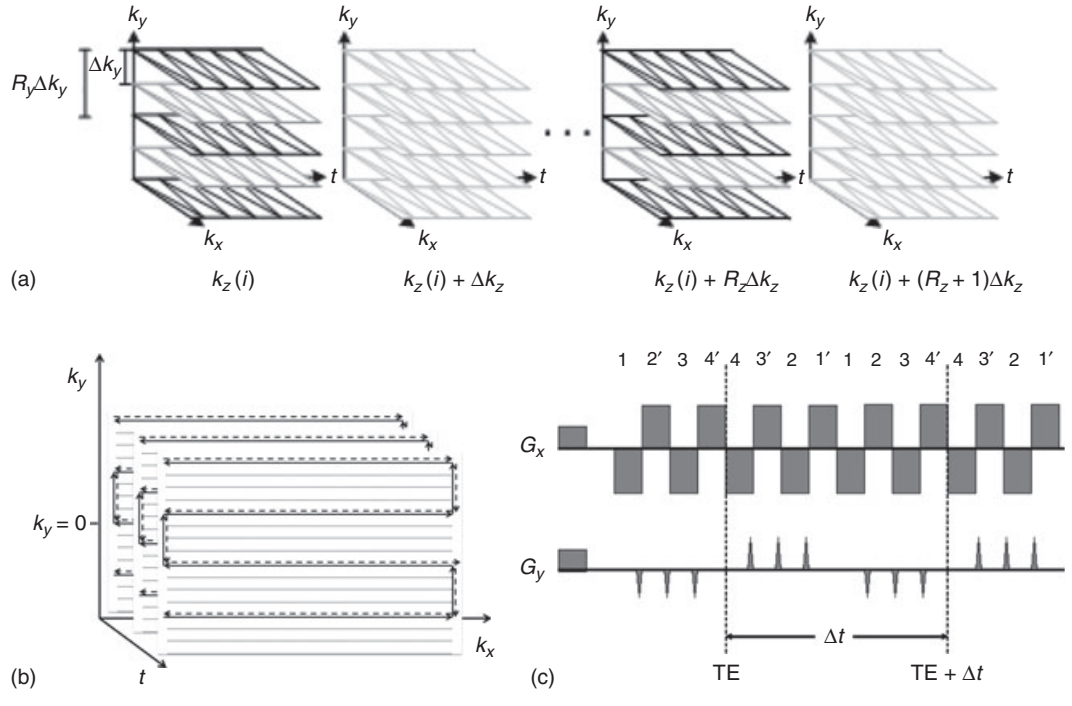

Figure 8. (a) The *k*-space trajectory for 3D-PEPSI with 2D parallel imaging is composed by parallel planes of zig-zag k_x–t trajectories. Δk_y and Δk_z determine the uniform sampling grid for k_y and k_z. The black lines represent the trajectory after down-sampling k_y and k_z by a factor R_y and R_z, respectively. (b) The k_x–k_y-space trajectory for single-shot 2D-PEPSI using fourfold acceleration with partial parallel imaging. The solid line represents the forward trajectory and the dashed line represents the reverse trajectory. (c) The gradient switching scheme for single-shot 2D-PEPSI shown in (b). The phase-encoding gradient blips are interleaved between the alternating readout gradients

As pointed out earlier, spiral MRSI requires *k*-space rewinding before the sampling of the next time point. This rewinding reduces sensitivity as the SNR is proportional to the square root of the sampling time, and the time needed for rewinding is wasted. Compared with phase-encoded MRSI and EPSI with ramp sampling, there is a theoretical reduction of sensitivity in spiral MRSI. On the other hand, given that the sampling density is higher in the center of *k*-space, even without the explicit use of variable density, the low *k*-space data will have a higher relative SNR upon reconstruction. When apodization is used, there is a further increase in SNR. In both cases, it is worth noting that the nonuniform SNR in *k*-space and apodization leads to correlation of the noise between different voxels.

Advanced Topics

Coil Arrays and Parallel Imaging

Parallel imaging using sensitivity encoding (SENSE)[47] and generalized autocalibrating of partially parallel acquisitions (GRAPPA)[48] (see ***CSI and SENSE CSI***) has been successfully applied to accelerate PEPSI. Standard coil arrays with 8–12 elements have enabled acceleration factors of 2–3 for 2D-PEPSI with scan times of 22–32 s,[18,20] and acceleration factors of 1.6 for high spatial resolution 3D-PEPSI with scan times of 16 min.[49] Up to a fivefold acceleration of 2D-PEPSI for scan times as short as 12 s was feasible using a 32-element coil array.[18,20] Up to an eightfold acceleration of 3D-PEPSI with 1 min scan times was demonstrated using 2D-SENSE using a 32-element coil array[19] (Figure 8). Regularization was performed by constraining the singular value decomposition of the encoding matrix to reduce the effect of low-value and overlapped coil sensitivities. The effects of spectral heterogeneity and discontinuities in coil sensitivity across the spectroscopic voxels were minimized by unaliasing the PSF to reduce the contamination from extracranial lipids.

Further acceleration of PEPSI by interleaving of undersampled phase encoding into the echo-planar spatial–spectral encoding scheme and SENSE reconstruction has enabled single-shot 2D metabolite mapping, albeit at a reduced spatial resolution and spectral width.[21] An alternative approach using PEPSI encoding along the readout direction and inverse imaging along the phase-encoding direction using a reconstruction method similar to that of magneto-encephalography (MEG) enabled single shot encoding with the full spectral bandwidth of conventional PEPSI.[50] This approach can be readily extended to inverse imaging along two spatial dimensions to achieve single-shot 3D metabolite mapping that can benefit from the development of increasingly larger radio frequency (RF) coil arrays, which may contain up to 90 or more coil elements. The price to pay for these extreme levels of acceleration is that the reconstruction has a spatially varying PSF that is dictated by the coil sensitivity maps. An intermediate approach between standard parallel imaging and inverse imaging was presented in the super-resolution sensitivity encoding (SURE-SENSE) PEPSI method,[51] where intravoxel coil sensitivity variations measured at high-spatial resolution were exploited to increase

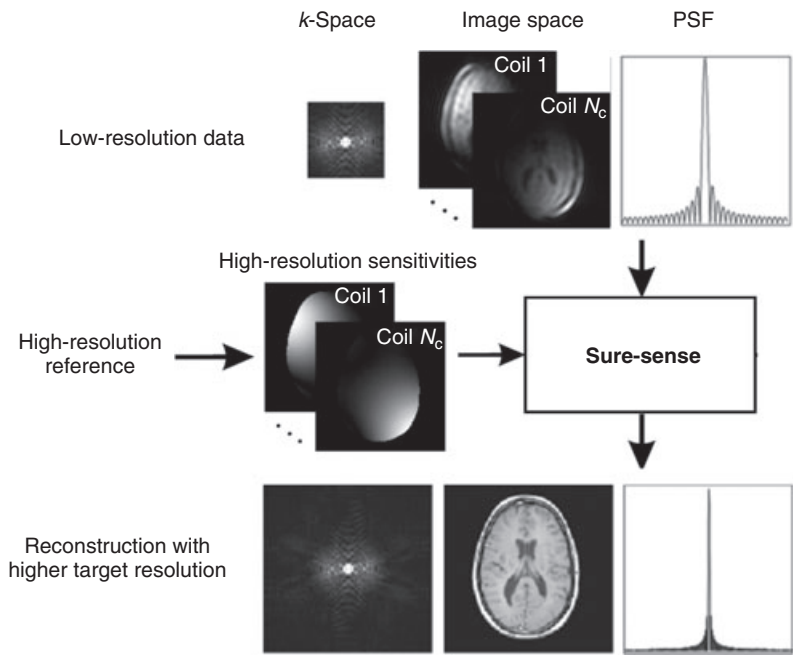

Figure 9. Conceptual illustration of the super-resolution parallel MRSI technique. The low-resolution multicoil data are combined into a single image with higher resolution by performing an intravoxel reconstruction with high spatial resolution coil sensitivity maps

the spatial resolution of a low-spatial resolution acquisition, using a regularized super-resolution reconstruction (Figure 9). SURE-SENSE enables acceleration along all spatial dimensions including the readout dimension for echo-planar trajectories. This is not feasible with standard parallel imaging techniques, and it is particularly useful for reducing contamination from peripheral lipid signals, which is one of the major challenges in short-TE MRSI.

Compressed Sensing

In vivo proton MRSI data are often confounded by limited spectral information due to susceptibility-related line broadening or short T_2 relaxation. For example, long TE data contain only a small number of spectral components that can be described with few parameters. Such spectra are called *sparse* and can in principle be acquired with fewer data points than traditional methods using undersampled acquisition and reconstruction methods such as compressed sensing (see ***Pulse sequences for hyperpolarized MRS***).[52] Compressed sensing can be applied to increase the spectral bandwidth when interleaving phase encoding into an echo-planar trajectory with random sampling along the phase-encoding dimensions to ensure that aliasing artifacts remain incoherent. Moreover, compressed sensing can be combined with other acceleration techniques to further increase the acceleration rate. For example, the combination of compressed sensing and parallel imaging that takes into consideration intra- and intercoil correlations was demonstrated to increase acceleration rates for PEPSI,[53] thereby enabling previously impractical combinations of total scan time, volumetric coverage, and spatial resolution.

Volume Prelocalization

The point-resolved spectroscopy (PRESS), stimulated echo acquisition mode (STEAM), and localized adiabatic spin-echo refocusing (LASER) methods provide robust prelocalization within a rectangular region of interest (see ***Single-Voxel MR Spectroscopy***). Lipid nulling using inversion recovery enables measurement of metabolite signals in the lateral cortices in close proximity to peripheral lipid-containing regions for whole brain echo-planar MRSI.[17] However, lipid nulling incurs an approximately 30% sensitivity loss in all metabolites at 3 T, and elevated lipid and macromolecular resonances that may be valuable for assessing brain lesions are not measurable. Outer volume suppression (OVS) using spatial presaturation maintains sensitivity at short-TE and has been successfully used for 2D and 3D PEPSI.[10,11,15,16] An iterative optimization approach has been developed to automatically place up to 16 OVS slices in peripheral regions using image-based segmentation of brain and peripheral regions.[54] Motivated by the increasing availability of statistical brain atlases for automated positioning of MRI slices and the proven high efficiency, robustness, and precision of this methodology, an automated atlas-based approach was developed for positioning up to 16 OVS slices in the brain using an affine transformation of optimally positioned OVS slices and the MRSI slab in atlas space.[55] In the future, a nonplanar geometry of automated OVS slice prescription from nonlinear transformation may be feasible using curved slice excitation with multidimensional RF pulses to further improve volume coverage in lateral brain regions.

Field Strength Dependence

Implementation of high-speed MRSI at ultrahigh field (7 T and beyond) is challenging due to limitations in gradient slew rates, which affect sensitivity and limits spectral widths. To maintain spectral bandwidth and SNR for PEPSI, it would be necessary to increase the slew rate proportional to B_0^2, which is neither feasible with current gradient technology nor safe due to the potential for peripheral nerve stimulation. The alternative is to increase ramp sampling at the expense of SNR and/or to employ spectral interleaving to increase the spectral bandwidth (see ***Direct Water–Fat Imaging Methods: Chemical Shift-Selective and Chemical Shift-Encoded MRI***). The increase in B_0 inhomogeneity at ultrahigh field (i.e., at 7 T and beyond) is a major challenge for shimming that limits the sensitive volume. Furthermore, spatial prelocalization becomes a major challenge at high field due to increased RF field (B_1) inhomogeneity, limited B_1 amplitudes due to power requirements, and increased specific absorption rates (SAR), which constrain RF pulse performance and can elongate the minimum TE and TR compared to 3 T. Already, parallel transmission techniques, which combine multicoil excitation and RF pulse design, have emerged as powerful tools to deal with B_1 inhomogeneities while controlling SAR at high field.

To assess sensitivity at different field strengths, the PEPSI technique has been implemented at 1.5, 3, 4, and 7 T on scanners sharing similar software and hardware platforms, using circularly polarized (CP or quadrature) and 8-channel phased-array (PA) head coils.[15] The SNR per unit volume and per unit time, and the intrinsic line-width (LW) of brain N-Acetyl-Aspartate (NAA), total Creatine (unphosphorylated plus phosphorylated; Cr), and Choline (Cho) were measured in a supraventricular para-axial slice location. Data were corrected for relaxation effects and processed with a time-domain matched filter adapted to each B_0. SNR and LW measured with PEPSI were very similar to PRESS spectroscopic imaging. SNR in central brain regions measured with the CP head coil increased nearly linearly with B_0, consistent with previous studies using conventional MRS and MRSI methods,[15] and theoretical expectations. For the PA coil, the SNR–B_0 relationship was less than linear but exhibited a substantial SNR increase compared to the CP coil. The LW measured in parts per million decreased with $B_{0,}$ resulting in an improved spectral resolution.

Selected Applications

Dynamic Measurements of Metabolic Changes

PEPSI enabled 2D regional mapping of dynamic metabolic changes on a time scale of several minutes in human brain in response to hyperventilation, a physiological challenge that decreases global blood flow,[56] and to the more subtle metabolic effects of caffeine ingestion.[57] The 2D distribution showing increasing brain lactate during hyperventilation was measured in five healthy subjects on a conventional clinical scanner equipped with a head surface coil PA. PEPSI images (nominal voxel size: 1.125 cm^3) from an axial section approximately 20 mm inferior to the intercommissural line were obtained during an 8.5 min baseline period of normocapnia, and during the final 8.5 min of a 10 min period of capnometry-controlled hyperventilation (end-tidal PCO_2 of 20 mmHg). The lactate/NAA signal increased significantly from baseline during hyperventilation for the insular cortex, temporal cortex, and occipital regions of both the right and left hemispheres, but not in the basal ganglia. Regional or hemispheric right-to-left differences were not found. The study extends previous work using single-voxel MR spectroscopy to dynamically study hyperventilation effects on brain metabolism.

Whole Brain Coverage

Maudsley and colleagues have developed clinically feasible whole brain metabolite mapping for brain using 3D EPSI at intermediate echo-times (70 ms) with scan times of 26 min,[17,58] and more recently at a short echo-time (20 ms) with scan times of 16 min.[49] Figure 10 shows examples of metabolite maps measured in a single subject at intermediate TE, and averaged results from a group study that reveals previously unattainable tissue contrast in metabolite maps. The fast acquisition speed of 3D PEPSI technique has been particularly suitable for metabolite mapping in children, e.g., in longitudinal studies in infants at high genetic risk for autism spectrum disorder (ASD).[1]

High Spatial Resolution

Voxel volumes on the order of 0.3 cc can be readily measured at 3 T[59], and the use of surface coils and array coils allows even smaller voxel volumes on the order of 0.1 cc, or smaller, in the cortex. The high sensitivity of ^{1}H-MRSI and the use of sensitive surface coil arrays in combination with high-speed MRSI enable metabolite mapping with spatial resolution approaching that of functional MRI, to delineate gray–white matter differences in metabolite concentrations. Figure 11 shows examples of mapping J-coupled resonances with 4.5 mm in-plane resolution using PEPSI at short echo-time (15 ms) in a healthy volunteer.[1] The combined Glutamate + Glutamine (Glu + Gln) map shows gray–white matter contrast, which follows the sulcal pattern seen in the corresponding high-resolution MRI. The Cr map also shows gray–white matter contrast. The Choline (Cho) map shows an inverse contrast and higher Cho concentration in anterior brain regions compared to the posterior brain.

Combination with 2D J-Resolved Acquisition

The Glu multiplet overlaps strongly with the Gln multiplet and macromolecules at 3 T and even at 4 T when line broadening is present. This makes it difficult to obtain independent concentration estimates for each of these molecules, although their sum (labeled Glx) can be estimated. The integration of 2D J-resolved acquisition using TE-averaging into 2D and 3D high-speed MRSI has been shown to enable selective measurement of Glu in clinically feasible scan times.[5,60] A comparison of TE-averaged 3D PEPSI with short TE 3D PEPSI at 3 T using an identical voxel size (1 cc) showed that despite a doubling of acquisition time for the TE-averaged PEPSI, the Cramer–Rao lower bounds (CRLBs) for Glu were significantly larger than for short TE PEPSI. This suggests that the increase in specificity for Glu comes at a cost of sensitivity.[1]

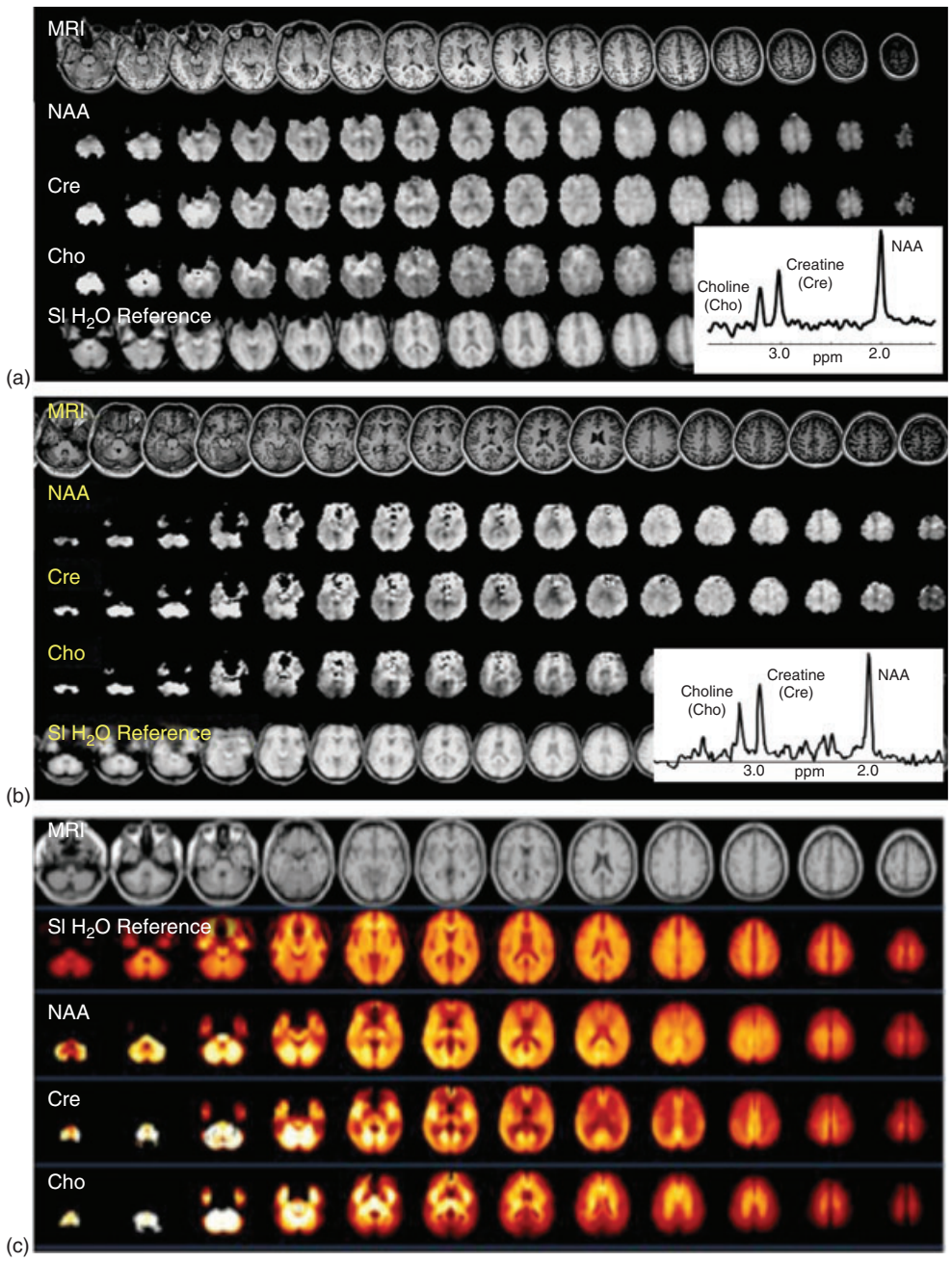

Figure 10. Whole brain mapping of metabolites using echo-planar spectroscopic imaging (EPSI) at 3 T.[17] (a) Single subject at intermediate echo time (70 ms), (b) single subject at short echo time (20 ms), and (c) group average from 47 female and 41 male subjects at intermediate echo time (70 ms). Spatial normalization was applied. Intermediate echo time data were acquired using a 12-channel coil and 26 min acquisition time, with $50 \times 50 \times 18$ *k*-space points interpolated to $64 \times 64 \times 32$ and $5.6 \times 5.6 \times 10$ mm (0.31 cc) voxel size. Short TE data were acquired in 15 min. (Reproduced with permission from Ref. 1. © John Wiley & Sons, Ltd., 2012)

Conclusions

High-speed ^{1}H-MRSI techniques are well suited to replace conventional phase-encoded ^{1}H-MRSI in the brain when acceptable magnetic field homogeneity can be achieved across large volumes. Shorter acquisition times and higher spatial resolution are realized using large-scale array coils and high field strength (3–7 T). Integration of parallel imaging and compressed sensing can reduce encoding times even further, which is advantageous for reducing motion sensitivity and for increasing volume coverage and spatial resolution, resulting in scan times of just a few minutes. The fast encoding speed enables monitoring of dynamic metabolic changes, and extends the application of 3D MRSI to patient populations such as infants, that are otherwise difficult to scan with conventional MRSI. It is anticipated that this technology will become increasingly available on modern MRI scanners for broader clinical applications to the brain and body.

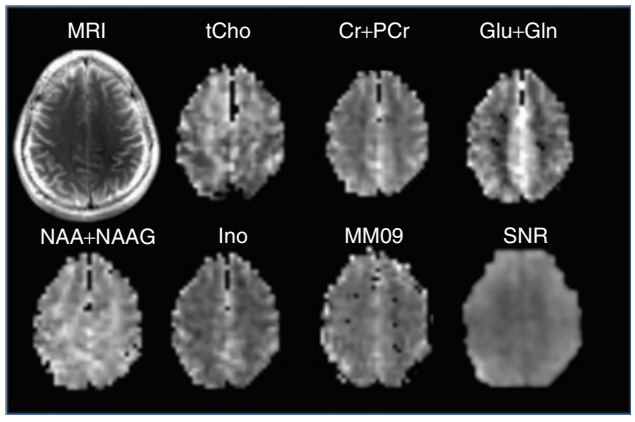

Figure 11. High spatial resolution mapping of J-coupled metabolites in human brain at 3 T using short TE (15 ms) proton echo-planar spectroscopic imaging (PEPSI). The high-resolution MRI, partial volume and relaxation-corrected metabolite images, and a map of the signal-to-noise ratio reported by LCModel fitting (slice mean SNR of NAA $=7.5 \pm 1.6$) are shown. Data were acquired with 4.5 mm in-plane resolution and 15 mm slice thickness (0.3 cc voxel size) in a supraventricular slice location using a 32-channel array coil and 32 min acquisition time. (Reproduced with permission from Ref. 1. © John Wiley & Sons, Ltd., 2012)

Acknowledgments

We gratefully acknowledge the contributions of our colleagues, former and present students, postdocs, and staff members who participated in the development and application of high-speed MRSI: Elena Ackley, Dr. Andrew Maudsley, Dr. Jeffrey Alger, Dr. Stephen R. Dager, Dr. Fa-Hsuan Lin, Dr. Ricardo Otazo, Dr. Shang-Yueh Tsai, Dr. Lawrence L. Wald, and Dr. Chenguang Zhao. The authors would gratefully acknowledge Dr. Shantanu Sarkar, who graciously permitted the use of texts and figures from his PhD dissertation in this article.

Biographical Sketches

Stefan Posse, Dipl. Phys, U. Cologne, Germany, 1986, Dr. phil. nat., Biomedical MR, U. Berne, Switzerland, 1990, Habilitation, University of Duesseldorf, Germany, 1999, Fogarty Fellow, National Institutes of Health, 1991–1994, Head of MR research, Forschungszentrum Jülich GmbH, Germany, 1995–1999, Assistant and Associate Professor, Wayne State University School of Medicine, 2000–2003. Currently, tenured Professor in the Departments of Neurology, Electrical and Computer Engineering, and Physics and Astronomy, University of New Mexico School of Medicine. 88 peer-reviewed publications, 13 issued patents, 3 book chapters, and over 260 published abstracts. Research specialties: high-speed MR spectroscopic imaging in the human brain, real-time functional MRI, BOLD contrast mechanisms and quantification, clinical applications of MR in neurological and psychiatric disease, and breast cancer.

Xiaoping Hu obtained his PhD in medical physics from the University of Chicago in 1988 and his postdoctoral training there from 1988 to 1990. From 1990 to 2002, he was in the faculty of the University of Minnesota. Since 2002, he has been Professor and Georgia Research Alliance Eminent Scholar in Imaging in the Wallace H. Coulter Joint Department of Biomedical Engineering at Georgia Tech and Emory University and director of Biomedical Imaging Technology Center at Emory University. He has worked on the development and biomedical application of magnetic resonance imaging and spectroscopy for more than three decades and has published 245 peer-reviewed journal articles.

Related Articles

Pulse sequences for hyperpolarized MRS; CSI and SENSE CSI; Spectral editing in MRS; 2D MRS; Direct Water–Fat Imaging Methods: Chemical Shift-Selective and Chemical Shift-Encoded MRI; Measuring Metabolite Concentrations I–Brain ^{1}H MRS; Single-Voxel MR Spectroscopy.

References

1. S. Posse, R. Otazo, S. R. Dager, and J. Alger, *J. Magn. Reson. Imaging*, 2013, **37**, 1301.
2. T. R. Brown, B. M. Kincaid, and K. Ugurbil, *Proc. Natl. Acad. Sci. U. S. A.*, 1982, **79**, 3523.
3. A. A. Maudsley, S. K. Hilal, W. H. Perman, and H. E. Simon, *J. Magn. Reson. (1969)*, 1983, **51**, 147.
4. D. Mayer, W. Dreher, and D. Leibfritz, *Magn. Reson. Med.*, 2000, **44**, 23.
5. R. Srinivasan, C. Cunningham, A. Chen, D. Vigneron, R. Hurd, S. Nelson, and D. Pelletier, *Neuroimage*, 2006, **30**, 1171.
6. U. Dydak, J. S. Xu, M. Marjanska, and S. Posse, *Proc: 19th Int. Soc. Magn.Reson. Med. (ISMRM) Annual Meeting*, 2011, 1428.
7. P. Mansfield, *Magn. Reson. Med.*, 1984, **1**, 370.
8. P. Webb, D. Spielman, and A. Macovski, *Magn. Reson. Med.*, 1989, **12**, 306.
9. S. Matsui, K. Sekihara, and H. Kohno, *J. Magn. Reson.*, 1985, **64**, 167.
10. S. Posse, C. DeCarli, and D. Le Bihan, *Radiology*, 1994, **192**, 733.
11. S. Posse, G. Tedeschi, R. Risinger, R. Ogg, and D. Lebihan, *Magn. Reson. Med.*, 1995, **33**, 34.
12. G. Metzger and X. P. Hu, *J. Magn. Reson.*, 1997, **125**, 166.
13. A. Ebel and A. A. Maudsley, *Magn. Reson. Imaging*, 2003, **21**, 113.
14. E. Adalsteinsson, P. Irarrazabal, S. Topp, C. Meyer, A. Macovski, and D. M. Spielman, *Magn. Reson. Med.*, 1998, **39**, 889.
15. R. Otazo, B. Mueller, K. Ugurbil, L. Wald, and S. Posse, *Magn. Reson. Med.*, 2006, **56**, 1200.
16. S. Posse, R. Otazo, A. Caprihan, J. Bustillo, H. Chen, P. G. Henry, M. Marjanska, C. Gasparovic, C. Zuo, V. Magnotta, B. Mueller, P. Mullins, P. Renshaw, K. Ugurbil, K. O. Lim, and J. R. Alger, *Magn. Reson. Med.*, 2007, **58**, 236.
17. A. A. Maudsley, C. Domenig, V. Govind, A. Darkazanli, C. Studholme, K. Arheart, and C. Bloomer, *Magn. Reson. Med.*, 2009, **61**, 548.
18. F. H. Lin, S. Y. Tsai, R. Otazo, A. Caprihan, L. L. Wald, J. W. Belliveau, and S. Posse, *Magn. Reson. Med.*, 2007, **57**, 249.
19. R. Otazo, S. Y. Tsai, F. H. Lin, and S. Posse, *Magn. Reson. Med.*, 2007, **58**, 1107.
20. S. Y. Tsai, R. Otazo, S. Posse, Y. R. Lin, H. W. Chung, L. L. Wald, G. C. Wiggins, and F. H. Lin, *Magn. Reson. Med.*, 2008, **59**, 989.
21. S. Posse, R. Otazo, S. Y. Tsai, A. E. Yoshimoto, and F. H. Lin, *Magn. Reson. Med.*, 2009, **61**, 541.
22. O. C. Andronesi, B. A. Gagoski, and A. G. Sorensen, *Radiology*, 2012, **262**, 647.
23. C. H. Cunningham, D. B. Vigneron, A. P. Chen, D. Xu, S. J. Nelson, R. E. Hurd, D. A. Kelley, and J. M. Pauly, *Magn. Reson. Med.*, 2005, **54**, 1286.
24. L. G. Hanson, K. Schaumburg, and O. B. Paulson, *Magn. Reson. Med.*, 2000, **44**, 412.

25. S. Posse, *Magn. Reson. Med.*, 1992, **25**, 12.
26. R. Pohmann, M. von Kienlin, and A. Haase, *J. Magn. Reson.*, 1997, **129**, 145.
27. J. G. Pipe and J. L. Duerk, *Magn. Reson. Med.*, 1995, **34**, 170.
28. A. Ebel and A. A. Maudsley, *Magn. Reson. Med.*, 2005, **53**, 465.
29. E. Adalsteinsson and D. M. Spielman, *Magn. Reson. Med.*, 1999, **41**, 8.
30. C. B. Ahn, J. H. Kim, and Z. H. Cho, *IEEE Trans. Med. Imaging*, 1986, **5**, 2.
31. C. H. Meyer, B. S. Hu, D. G. Nishimura, and A. Macovski, *Magn. Reson. Med.*, 1992, **28**, 202.
32. D. M. Spielman, J. M. Pauly, and C. H. Meyer, *Magn. Reson. Med.*, 1995, **34**, 388.
33. C. J. Hardy and H. E. Cline, *J. Appl. Phys.*, 1989, **66**, 1513.
34. C. H. Meyer, J. M. Pauly, and A. Macovski, *Proc: 4th Int. Soc. Magn. Reson. Med. (ISMRM) Annual Meeting*, 1996, Vol. **1**, 392.
35. K. F. King, T. K. Foo, and C. R. Crawford, *Magn. Reson. Med.*, 1995, **34**, 156.
36. J. R. Liao, J. M. Pauly, and N. J. Pelc, *Magn. Reson. Med.*, 1997, **38**, 246.
37. G. H. Glover, *Magn. Reson. Med.*, 1999, **42**, 412.
38. J. D. O'Sullivan, *IEEE Trans. Med. Imaging*, 1985, **44**, 200.
39. J. I. Jackson, C. H. Mayer, D. G. Nishimura, and A. Macovski, *IEEE Trans. Med. Imaging*, 1991, **10**, 473.
40. D. L. Parker, G. T. Gullberg, and P. R. Frederick, *Med. Phys.*, 1987, **14**, 640.
41. H. R. Brooker, T. H. Mareci, and J. T. Mao, *Magn. Reson. Med.*, 1987, **5**, 417.
42. P. M. R. M. Garwood and K. Ugurbil, *J. Magn. Reson.*, 1987, **75**, 244.
43. E. Adalsteinsson, J. Star-Lack, C. H. Meyer, and D. M. Spielman, *Magn. Reson. Med.*, 1999, **42**, 314.
44. X. Hu, M. Patel, and K. Ugurbil, *J. Magn. Reson. B*, 1994, **103**, 30.
45. G. Metzger, S. Sarkar, X. Zhang, K. Heberlein, M. Patel, and X. Hu, *Magn. Reson. Imaging*, 1999, **17**, 435.
46. S. Sarkar, K. Heberlein, and X. Hu, *Magn. Reson. Imaging*, 2002, **20**, 743.
47. K. P. Pruessmann, M. Weiger, M. B. Scheidegger, and P. Boesiger, *Magn. Reson. Med.*, 1999, **42**, 952.
48. M. A. Griswold, P. M. Jakob, R. M. Heidemann, M. Nittka, V. Jellus, J. Wang, B. Kiefer, and A. Haase, *Magn. Reson. Med.*, 2002, **47**, 1202.
49. X. Q. Ding, A. A. Maudsley, M. Sabati, S. Sheriff, P. R. Dellani, and H. Lanfermann, *Magn. Reson. Med.*, 2015, **73**, 921.
50. F. Lin, S. Y. Tsai, Y. R. Lin, R. Otazo, G. Wiggins, L. L. Wald J. Belliveau, and S. Posse, *Proc: 16th Int. Soc. Magn. Reson. Med. (ISMRM) Annual Meeting*, 2008, 595.
51. R. Otazo, F. H. Lin, G. Wiggins, R. Jordan, D. Sodickson, and S. Posse, *Neuroimage*, 2009, **47**, 220.
52. M. Lustig, D. Donoho, and J. M. Pauly, *Magn. Reson. Med.*, 2007, **58**, 1182.
53. R. Otazo, D. Sodickson, A. Yoshimoto, and S. Posse, *Proc: 17th Int. Soc. Magn.Reson. Med. (ISMRM) Annual Meeting*, 2009, 331.
54. M. Martinez-Ramon, A. Gallardo-Antolin, J. Cid-Sueiro, G. L. Heileman, K. T. Yung, W. Zheng, C. Zhao, and S. Posse, *Magn. Reson. Med.*, 2010, **63**, 592.
55. K. T. Yung, W. Zheng, C. Zhao, M. Martinez-Ramon, A. van der Kouwe, and S. Posse, *Magn. Reson. Med.*, 2011, **66**, 911.
56. S. Posse, D. Sr, T. L. Richards, C. Yuan, R. Ogg, A. A. Artru, H. W. MullerGartner, and C. Hayes, *Magn. Reson. Med.*, 1997, **37**, 858.
57. S. R. Dager, M. E. Layton, W. Strauss, T. L. Richards, A. Heide, S. D. Friedman, A. A. Artru, C. E. Hayes, and S. Posse, *Am. J. Psychiatr.*, 1999, **156**, 229.
58. A. A. Maudsley, A. Darkazanli, J. R. Alger, L. O. Hall, N. Schuff, C. Studholme, Y. Yu, A. Ebel, A. Frew, D. Goldgof, Y. Gu, R. Pagare, F. Roulsseau, K. Sivasankaran, B. J. Soher, P. Weber, K. Young, and X. Zhu, *NMR Biomed.*, 2006, **19**, 492.
59. A. A. Maudsley, C. Domenig, and S. Sheriff, *NMR Biomed.*, 2010, **23**, 251.
60. K. Yung, S. Y. Tsai, F. H. Lin, P. G. Henry, A. Yoshimoto, and S. Posse, *Proc: 17th Int. Soc. Magn. Reson. Med. (ISMRM) Annual Meeting*, 2009, 4314.